Title
Numerical predictions of shear stress and cyclic stretch in pulmonary hypertension due to left heart failure

Journal
Biomechanics and Modeling in Mechanobiology, 21(1)

ISSN
1617-7959

Authors
Bartolo, Michelle A
Qureshi, M Umar
Colebank, Mitchel J
et al.

Publication Date
2022-02-01

DOI
10.1007/s10237-021-01538-1

Peer reviewed

HHS Public Access

Author manuscript

Biomech Model Mechanobiol. Author manuscript; available in PMC 2023 May 11.

Published in final edited form as:

Biomech Model Mechanobiol. 2022 February ; 21(1): 363–381. doi:10.1007/s10237-021-01538-1.

Numerical predictions of shear stress and cyclic stretch in pulmonary hypertension due to left heart failure

Michelle A. Bartolo[1], **M. Umar Qureshi**[1], **Mitchel J. Colebank**[2], **Naomi C. Chesler**[2], **Mette S. Olufsen**[3]

[1] Department of Mathematics, North Carolina State University, Raleigh, NC 27695, USA

[2] Edwards Lifesciences Foundation Cardiovascular Innovation and Research Center, University of California, Irvine, CA 92697, USA

[3] Department of Mathematics, North Carolina State University, Raleigh, NC 27607, USA

Abstract

Isolated post-capillary pulmonary hypertension (Ipc-PH) occurs due to left heart failure, which contributes to 1 out of every 9 deaths in the United States. In some patients, through unknown mechanisms, Ipc-PH transitions to combined pre-/post-capillary PH(Cpc-PH) and is associated with a dramatic increase in mortality. Altered mechanical forces and subsequent biological signaling in the pulmonary vascular bed likely contribute to the transition from Ipc-PH to Cpc-PH. However, even in a healthy pulmonary circulation, the mechanical forces in the smallest vessels (the arterioles, capillary bed, and venules) have not been quantitatively defined. This study is the first to examine this question via a computational fluid dynamics model of the human pulmonary arteries, arterioles, venules, and veins. Using this model, we predict temporal and spatial dynamics of cyclic stretch and wall shear stress with healthy and diseased hemodynamics. In the normotensive case for large vessels, numerical simulations show that large arteries have higher pressure and flow than large veins, as well as more pronounced changes in area throughout the cardiac cycle. In the microvasculature, shear stress increases and cyclic stretch decreases as vessel radius decreases. When we impose an increase in left atrial pressure to simulate Ipc-PH, shear stress decreases and cyclic stretch increases as compared to the healthy case. Overall, this model predicts pressure, flow, shear stress, and cyclic stretch that providing a way to analyze and investigate hypotheses related to disease progression in the pulmonary circulation.

Keywords

Pulmonary hypertension; Micro-circulation; Wall shear stress; Cyclic stretch; Left heart disease; Computational modeling; Pulse wave propagation

1 Introduction

Chronic left heart failure (LHF) impacts nearly 5.9 million adults and contributes to 1 out of 9 deaths in the United States (Mozaffarian et al. 2016). About 60–80% of

✉ Mette S. Olufsen msolufse@ncsu.edu.

patients with LHF develop pulmonary hypertension (PH-LHF) (Ghio et al. 2001; Lam et al. 2009), which dramatically increases morbidity and mortality (Guazzi and Borlaug 2012; Guglin and Khan 2010; Ramu and Thenappan 2016). According to the 2019 World Health Organization guidelines, diagnosis of PH-LHF (classified under group-II PH) (Simonneau et al. 2019) requires a mean pulmonary artery pressure (mPAP) > 20mmHg and a pulmonary capillary wedge pressure (PCWP) > 15mmHg (Simonneau et al. 2019). The disease begins with isolated post-capillary PH (Ipc-PH), a passive process characterized by sustained elevated left-atrial and pulmonary venous pressures, leading to increases in pulmonary arterial pressure. The increased pressure progressively remodels the vasculature, often starting in the small vessels and propagating to the main pulmonary artery (MPA) (Ravi et al. 2013). In some patients, through unknown mechanisms, Ipc-PH transitions to combined pre-/post-capillary PH (Cpc-PH), which significantly worsens the disease prognosis. The increase in pulmonary vascular resistance (PVR) marks a change from reversible to the irreversible stage, significantly increasing the mortality risk (Gerges et al. 2015; Miller et al. 2013). Altered mechanical forces and subsequent vasoactive signaling in pulmonary vascular bed may contribute to the transition from Ipc-PH and Cpc-PH. However, mechanical forces in the small pulmonary arterioles and venules have not yet been quantitatively studied, even in the healthy pulmonary vasculature. A crucial precursor to investigating mechanobiological mechanisms of disease progression is quantifying the dynamic vascular mechanical environment in both healthy and diseased states. This study examines the time course and distribution of wall shear stress (WSS) and cyclic stretch (CS) in the pulmonary circulation in the first stages of Ipc-PH. We elevate left atrial pressure and decrease cardiac output to simulate the progression of Ipc-PH to enhance our understanding of how mechanical stimuli act on the vasculature and provide a basis for studying the PH-LHF progression.

WSS (g/cms^2) is a a key driver of vascular remodeling that may be critical to PH-LHF progression (Moraes and Loscalzo 1997). It is defined as the tangential force exerted by the blood flow per unit surface area of tunica intima (i.e., the interior surface blood vessels covered with a thin layer endothelial cells called the endothelium) (Paszkowiak and Dardik 2003). WSS is a local quantity and not an integrated property of the entire intima, yet it is intimately connected to the momentum exchange at the surface (Paszkowiak and Dardik 2003). As such, WSS is directly proportional to blood flow velocity and viscosity, and indirectly proportional to vessel radius cubed (Paszkowiak and Dardik 2003). Endothelial cell signaling in response to altered WSS is associated with vascular remodeling, which may lead to the worsening of PH-LHF (Roux et al. 2020). WSS is also a predictor of endothelial function due to its role in stimulating the production, release, and penetration of nitric oxide (NO) from the intima to the smooth muscle cells in the media. NO acts as a vital protective agent that maintains hemodynamic homeostasis by regulating vascular wall mechanics (Michel and Paul 2010). Specifically, its production during periods of high flow rate leads to vasodilation, which maintains PVR within baseline values.

CS(%) is another physiological quantity that plays a role in endothelial function. Decreased CS stimulates vasoconstriction via increased endothelin-1 (ET-1) and decreased endothelial nitric oxide synthase (eNOS) (van Duin et al. 2019). In vascular smooth muscle cells,

CS causes cell cycle arrest by elongating and realigning cells in the direction of stretch (Barron et al. 2007). Combined with increased blood pressure and transmural stress, these changes result in thickening of the vascular wall, increased media-to-lumen ratio, and decreased lumen diameter. The combination of these multiple alterations to the vascular structure leads to increases in PVR and decreases in the arterial compliance (Birukov 2009). Thus, understanding the role of WSS and CS within the pulmonary circulation and the relationship between these two quantities may give insight into the pathogenesis of PH and other cardiovascular diseases.

It is difficult to approximate WSS and CS in vivo as these measurable hemodynamic quantities cannot quantitatively define shearing forces or separate their effects from the other physical parameters of the hemodynamic system (Papadaki and Mclntire 1999). However, computational fluid dynamics (CFD) provides a comprehensive theoretical framework for determining WSS magnitude and time course. Numerous mathematical models have been used to predict pressure and flow waveforms in the pulmonary arteries and veins (Blanco and Feijóo 2010; Mynard and Smolich 2015; Olufsen et al. 2012; Clark and Tawhai 2018; Chambers et al. 2020; Spilker et al. 2007), and some (Davies 2009; Reymond et al. 2011, 2012; Zambrano et al. 2018; Yang et al. 2019) have attempted to predict shear stress. Most of these studies predict two shear stress quantities: the time averaged WSS (TAWSS) and an oscillatory shear stress index (OSI), not quantifying CS or differentiating the response between large and small arteries, and veins. While these detailed predictions are excellent at examining the global environment, they do not predict microcirculatory and venous WSS or CS or their relationships with large arterial hemodynamics.

In this study, we develop a one-dimensional fluid dynamic model of the pulmonary circulation including both arteries and veins. We use a numerical algorithm to predict the pressure drop, wave propagation, and magnitude and time course of WSS and CS (Qureshi et al. 2014). The model includes large and small blood vessels capturing vessels with radii from cm to − μm. This variation in spatial scale allows quantification and exploration of system dynamics and mechanistic relationships (e.g., between microcirculatory and large arterial WSS or CS) at several levels of the pulmonary circulation (Selzer 1992).

Our model predicts these quantities in a multiscale model in which the geometry for the large arteries and veins is extracted from a computed tomography (CT) image from a healthy human subject, and the small vessels are represented by structured trees with dimensions informed by literature data. This allows us to study the distal vasculature in detail by predicting pressure, flow, WSS, and CS waveforms throughout the simulated network. To compare previous results from 3D studies (Zambrano et al. 2018; Tang et al. 2012; Yang et al. 2019), we also compute a 1D-TAWSS and 1D-OSI. We compute these quantities in the pulmonary circulation, studying both healthy and disease hemodynamics by increasing left atrial pressure and decreasing volumetric flow rate. This allows us to learn more about mechanobiological mechanisms in Ipc-PH. Investigation of these quantities in healthy and diseased states is an essential step for providing an understanding of disease mechanisms in PH-LHF patients.

2 Methods

The geometry of the large arteries and veins is determined from segmenting a computed tomography (CT) image, and the small vessels are represented by structured trees, parameterized using literature data. In the network of large and small vessels, we conduct 1D fluid dynamics simulations predicting flow, pressure, WSS, and CS using an inflow waveform specified from data. To study effects associated with the onset of Ipc-PH, we run simulations elevating left atrial pressure and reducing cardiac output. The latter is done by scaling the measured inflow waveforms. This section describes the network geometry, the 1D fluid dynamics model, and metrics, such as WSS and CS.

2.1. Network geometry

Vessel dimensions and network connectivity are extracted from CT chest images from a healthy 67-year-old female volunteer (Wilson et al. 2013)[1]. The geometric reconstruction of the first three generations of arteries and first generation of veins were generated using the open-source segmentation software 3DSlicer[2] (see Fig. 1). We used the vascular modeling toolkit (VMTK)(Antiga et al. 2008) to obtain cartesian loci tracing each vessel's center-lines within the network and measuring the associated radii. VMTK generates a pointcloud, which enables the network topology quantification in the form of connectivity matrices, and vessel's lengths computation by summing over the point-wise L_2 norms between successive center-line coordinates (Colebank et al. 2019). Table 2 lists the lengths and radii for all vessels in the network. To satisfy the topological equivalence of the connected arterial-venous structured trees, we set the same distal radii for the large terminal arteries (RIA, RTA, LIA, and LTA) and their mirroring veins (RSV, RIV, LSV, and LIV) (Qureshi et al. 2014).

Asymmetrically binary structured trees (Olufsen et al. 2000) (shown in Fig. 1) are generated using physiology-based scaling laws. At each junction, the daughter vessel radii and lengths are scaled by factors α and β to the parent vessel, i.e.,

$$r_{d_1} = \alpha r_p,\ r_{d_2} = \beta r_p,\ L_{(d_1,d_2)} = l_r r_{(d_1,d_2)},$$

where $\alpha, \beta < 1$ and $\alpha + \beta \geq 1$. Scaling parameters, along with a prescribed minimum radius $r_{\min}$, determine the number of generations and vascular bed density encompassing the small arteries, arterioles, veins, and venules. Values for α and β are taken from the study by Chambers et al. (2020).

2.2. Mathematical model

This study uses a 1D fluid dynamics network model, previously developed by Qureshi et al. (2014), to compute blood flow, blood pressure, and area deformation throughout the pulmonary network (see Fig. 1). This model delineates the hemodynamic domain into two sub-domains: a) a large vessel domain consisting of main arteries and veins extracted from

[1] Available from open-source Simvascular platform http://simvascular.github.io/clinicalCase4.html.
[2] https://www.slicer.org/

a CT image, and b) a small vessel domain, composed of pre-capillary arterioles and venules generated using a two-sided morphology-based binary structured tree model. As noted earlier, the geometry of the large vessels is extracted from data, and the model is driven by a measured flow waveform. In all vessels in this network, we predict pressure, volumetric flow, and cross-sectional area waveforms. Mathematically, the large vessels belong to a nonlinear computational domain, requiring a numerical solution of the governing fluid equations, whereas the small vessels constitute a linearized analytical domain that combines exact solutions of governing fluid equations with a recursive algorithm. Below we describe the fluid dynamics modeling, resulting equations for the large and small vessels, as well as boundary conditions needed to predict the hemodynamic quantities of interest for this study.

2.2.1. Large vessel fluid dynamics—In large vessels, inertia dominates the blood flow dynamics; thus, pressure-flow relations can be determined from solving the Navier-Stokes equations in one dimension. Similar to our previous studies (Olufsen et al. 2000; Qureshi et al. 2014), we compute blood pressure p(mmHg), flow $q\left(\text{cm}^3/\text{s}\right)$, and dynamic cross-sectional area $A\left(\text{cm}^2\right)$ throughout the network. Each vessel is modeled as an axisymmetric tube with a circular cross-section and impermeable wall. We assume that the blood is Newtonian, and the flow is incompressible, irrotational, and laminar. We account for the blood-wall interaction via the no-slip condition, ensuring that the blood flow velocity at the inner wall surface is same as the velocity of transverse wall motion. To obtain a 1D model, we impose the boundary layer condition by Olufsen et al. (2000)

$$u_x(r,x,t)=\begin{cases}\overline{u}, & r<R-\delta\\ \dfrac{\overline{u}(R-r)}{\delta}, & R-\delta<r\le R\end{cases} \tag{2.1}$$

where $u_x(r,x,t)$ is the axial velocity, and $\overline{u}_x$ is the averaged velocity outside of the boundary layer of thickness $\delta=\sqrt{\frac{\upsilon T}{2\pi}}$ (cm) computed as a function of T(s), the length of the cardiac cycle, and $\mu_L\left(\text{cm}^2/\text{s}\right)$ is the kinematic viscosity, μ_L is the viscosity, and ρ is the density. The boundary layer provides a flat axial velocity profile characterizing the inertiadominant flow in the large vessels consistent with (Nichols et al. 1991; Pedersen 1993; Pedersen et al. 1993).

We obtain the conservation of mass and balance of momentum by averaging the 1D Navier-Stokes equations, giving

$$\frac{\partial A}{\partial t}+\frac{\partial q}{\partial x}=0,\ \frac{\partial q}{\partial t}+\frac{\partial}{\partial x}\left(\frac{q^2}{A}\right)+\frac{A}{\rho}\frac{\partial p}{\partial x}=-\mathscr{F}\frac{q}{A}, \tag{2.2}$$

where x(cm) and t(s) are spatial and temporal coordinates, respectively, and $\mathscr{F}=2\pi\upsilon/\delta$ is a frictional term. To close the system of equations, we assume a linear elastic relationship between pressure and cross-sectional area of the form

$$p(x,t)-p_0=\frac{4}{3}\frac{Eh}{r_0}\left(\sqrt{\frac{A}{A_0}}-1\right) \tag{2.3}$$

where E(mmHg) is Young's modulus, h(cm) is vessel wall thickness, p_0 is a reference pressure (mmHg), and A_0(cm^2) is the corresponding cross-sectional area. As suggested by Krenz and Dawson (2003), for the large arteries and veins, the vascular stiffness is assumed constant, i.e., we assume that $Eh/r_0 = k_3$. For the large arteries (la), we adopt the value reported by Paun et al. (2020), imposing $k_3^{la} = 1 \times 10^5$, and for the large veins (lv), we let $k_3^{lv} = 1.25 \times k_3^{la}$, making the pulmonary veins stiffer than the arteries (Banks et al. 1978; Wiener et al. 1966; Caro and Saffman 1965; Yen and Foppiano 1981; Maloney et al. 1970).

Since our system of equations is hyperbolic, we specify boundary conditions at the inlet and outlet of each vessel. At the inlet to the pulmonary circulation, i.e., the MPA, we specify a flow waveform extracted from magnetic resonance imaging, following the method used in Colebank et al. (2021) (Fig. 1). We digitize an average flow waveform, available from Simvascular, using Graphclick, providing an inflow boundary condition. At network junctions, we enforce flow conservation and pressure continuity

$$q_p(l_p, t) = q_{d_1}(0, t) + q_{d_2}(0, t) \tag{2.4}$$

$$p_p(l_p, t) = p_{d_1}(0, t) = p_{d_2}(0, t), \tag{2.5}$$

where the subscripts p, d_1, d_2 specify parent and daughter vessels and l_p specifies the length of the parent vessel. The outflow from the large terminal arteries and the inflow into the corresponding large terminal veins are obtained by coupling these vessels in series to two-sided arterial and venous structured trees. At the outflow of the large veins, a constant pressure is specified, corresponding to the mean left atrial pressure. We consider this to be the left atrium filling pressure. Since blood flows relatively freely into the left atrium, setting the pressure to a constant low value is reasonable. Additionally, fixing a constant pressure ensures a pressure gradient throughout the system that drives the blood flow. To simulate Ipc-PH progression, we increase the left atrial pressure with values ranging from 2 to 20 mmHg and decrease cardiac output by scaling the inflow profile by factors between 0.1 and 1.

2.2.2. Small vessel fluid dynamics—In the small vessels, viscous effects are dominant, so we can ignore the nonlinear inertial terms. As described in detail in Olufsen et al. (2000), Qureshi et al. (2014), the momentum equation in the axial direction is given by

$$\frac{\partial u_x}{\partial t} + \frac{1}{\rho}\frac{\partial p}{\partial x} = \frac{v}{r}\frac{\partial}{\partial r}\left(r\frac{\partial u_x}{\partial r}\right), \tag{2.6}$$

and the continuity equation is

$$C\frac{\partial p}{\partial t} + \frac{\partial q}{\partial x} = 0,\ C = \frac{\partial A}{\partial p} = \frac{3A_0 r_0}{2Eh}\left(1 - \frac{3pr_0}{4Eh}\right)^{-3} \approx \frac{3A_0 r_0}{2Eh} \tag{2.7}$$

As noted in several studies that analyze properties of small pulmonary arteries and veins, e.g., (Stack et al. 2014; Sicard et al. 2017; Townsley 2012; Segers et al. 1998; Stergiopulos et al. 1992; Westerhof et al. 1969; Sobin et al. 1977), the amount of collagen increases as the

vessels get smaller and thus, vessel stiffness increases. To model this, similar to our previous studies e.g., (Qureshi et al. 2014; Colebank et al. 2021; Chambers et al. 2020), we assume that

$$\frac{Eh}{r_0} = k_1 \exp(k_2 r_0) + k_3, \tag{2.8}$$

where k_1, k_2, and k_3 are parameters. This equation states that Young's modulus times the wall thickness relative to the unstressed radius increases as the vessels get smaller. For the small arteries and arterioles, we adapt values reported by Colebank et al. (2021): $k_1^{\text{art}} = 2.6 \times 10^5 \left(\text{g/cm/s}^2 \right)$, $k_2^{\text{art}} = -14\ \text{cm}^{-1}$, and $k_3^{\text{art}} = 1 \times 10^5 \left(\text{g/cm/s}^2 \right)$. These values are chosen to enforce continuity between the large and small vessels. Similar to the large vessels, we assume that the small pulmonary veins are stiffer than the arteries (Banks et al. 1978; Wiener et al. 1966), and we model this by increasing $k_i^{\text{ven}} = 1.25 \times k_i^{\text{art}}, i = 1,3$ (Wiener et al. 1966).

Assuming periodicity, flow and pressure can be written as $q(x,t) = Q(x)e^{i\omega t}$ and $p(x,t) = P(x)e^{i\omega t}$. Using this decomposition, we rewrite the momentum and continuity equations as

$$i\omega Q + \frac{A_0(1 - F_J)}{\rho} \frac{\partial P}{\partial x} = 0, \ F_J = 2J_1(w_0)/w_0 J_0(w_0) \tag{2.9}$$

$$i\omega C P + \frac{\partial Q}{\partial x} = 0, \tag{2.10}$$

where $J_i(w_0), i = 0,\ 1$ are the first and second order Bessel functions, and $w_0 = i^3 r_0^2 \omega/\mu$ is the Womersley number. Since the effects of blood viscosity become more significant as the vessel size decreases, as suggested by Pries et al. (1992), we compute small vessel viscosity μ_s as a function of the unstressed vessel radius r_0.

$$\mu_s(r_0) = \left[1 + (\mu_{0.45} - 1) \left(\frac{2r_0}{2r_0 - 1.1} \right)^2 \right] \left(\frac{2r_0}{2r_0 - 1.1} \right)^2 / 3.2 \tag{2.11}$$

$$\mu_{0.45}(r_0) = 6e^{-0.17 r_0} + 3.2 - 2.44 e^{-0.12 r_0^{0.645}}, \tag{2.12}$$

where $\mu_{0.45}(r_0)$ is the relative viscosity at a hematocrit level of 0.45 and 3.2 is the apparent viscosity limit, which provides large arterial viscosity when r_0 is large (Pries et al. 1992). Since this is a relative viscosity, we scale our structured tree viscosity by this function. Differentiating equation (2.10) with respect to x and substituting the result into equation (2.9) gives a wave equation of the form

$$\frac{\omega^2}{c^2} Q + \frac{\partial^2 Q}{\partial x^2} = 0 \text{ or } \frac{\omega^2}{c^2} P + \frac{\partial^2 P}{\partial x^2} = 0 \tag{2.13}$$

where $c = \sqrt{A_0(1 - F_J)/\rho C}$ is the wave propagation velocity. The solution to these equations is given by

$$Q = a\cos\left(\frac{\omega x}{c}\right) + b\sin\left(\frac{\omega x}{c}\right) \tag{2.14}$$

$$\begin{aligned} P &= ig_\omega{}^{-1}\left(-a\sin\left(\frac{\omega x}{c}\right) + \cos\left(\frac{\omega x}{c}\right)\right), \\ g_\omega &= \sqrt{\frac{CA_0(1 - F_J)}{\rho}}. \end{aligned} \tag{2.15}$$

We relate the flow and pressure at both ends of each vessel and compute the admittance of each structured tree to find a boundary condition that connect the large and small arteries and veins. A complete derivation of the admittance matrices through circuit theory can be found in the Appendix and in Qureshi et al. (2014).

2.2.3. Wall shear stress (WSS)—Large vessels. The shear stress, τ_w, that the fluid exerts on the vessel wall can be computed from the boundary layer from Eq. (2.1), giving us

$$\tau_w = -\mu\frac{\partial u_x}{\partial r} \tag{2.16}$$

$$= \begin{cases} 0, & r < R - \delta \\ \dfrac{\mu\bar{u}_x}{\delta}, & R - \delta < r \le R \end{cases} \tag{2.17}$$

where $\bar{u}_x = q/A$.

Small vessels.: To compute the shear stress in the small vessels, we assume that the driving pressure is oscillatory in time, consistent with the pumping action of the heart. We assume that this driving force consists of a constant part that does not vary in time, and an oscillatory part that moves the fluid back and forth over each cycle (Zamir and Budwig 2002). We refer to the combination of the two components as pulsatile flow. The steady and oscillatory components of pressure and axial velocity are denoted by

$$p(x,t) = p_s(x) + p_\phi(x,t), \text{ and } u(r,t) = u_s(r) + u_\phi(r,t).$$

Because of the independence of oscillatory and steady flow, the relationship between the pressure gradients is given by

$$k(t) = k_s + k_\phi(t), \tag{2.19}$$

where $\frac{dp}{dt} = k(t)$, $k_\phi(t) = k_s e^{i\omega t}$, and $u_\phi(r,t) = U_\phi(r)e^{i\omega t}$. Substituting these expressions into Equation (2.6) gives

$$\frac{\partial^2 U_\phi}{\partial r^2} + \frac{1}{r}\frac{\partial U_\phi}{\partial r} - \frac{i\Omega^2}{a^2}U_\phi(r) = \frac{k_s}{\mu} \tag{2.20}$$

where $\Omega = R\sqrt{\frac{\rho\omega}{\mu}}$, R is the tube radius, and μ is radius dependent viscosity. The solution is given by

$$U_\phi = \frac{ik_s R^2}{\mu\Omega^2}\left(1 - \frac{J_0(\zeta)}{J_0(\Lambda)}\right), \tag{2.21}$$

where $\zeta(r) = \Lambda\frac{r}{R}$ and $\Lambda = \left(\frac{i-1}{\sqrt{2}}\right)\Omega$. To find the oscillatory volumetric flow rate q_ϕ through a tube, we integrate the oscillatory velocity over a cross-section of the tube

$$\begin{aligned} q_\phi(t) &= \int_0^R 2\pi r u_\phi(r,\ t)dr \\ &= \frac{i\pi k_s R^4}{\mu\Omega^2}\left(1 - \frac{2}{\Lambda}\frac{J_1(\Lambda)}{J_0(\Lambda)}\right)e^{i\omega t}. \end{aligned}$$

As the fluid moves back and forth due to an oscillatory pressure gradient, the shear stress exerted by the fluid on the tube wall is given by

$$= \frac{-\mu\Lambda}{\pi R^3}\frac{J_1(\Lambda)}{J_0(\Lambda)\ -\ \frac{2}{\Lambda}J_1(\Lambda)}q_\phi. \tag{2.22}$$

$$\text{TAWSS} = \frac{1}{T}\int_0^T |\tau_w| dt. \tag{2.23}$$

To compare our results to 3D studies, we compute one-dimensional analogies to TAWSS and OSI. We compute TAWSS by finding

The oscillatory shear index (OSI) is a dimensionless metric that characterizes if WSS is aligned with TAWSS. It is computed as

$$\text{OSI} = 0.5\left(1 - \frac{\left|\int_0^T \tau_w\ dt\right|}{\int_0^T |\tau_w|\ dt}\right), \tag{2.24}$$

agreeing with previous definitions (He and Ku 1996; Stalder et al. 2008; Tang et al. 2011). This allows us to find the mean WSS over the pulzation, which in turn exhibits the magnitude of oscillation of the WSS.

We also quantify CS in order to develop an understanding of how diameter and circumferential stretch are related. To do this, we calculate

$$\text{CS} = \frac{r(x)\ -\ r_0(x)}{r_0(x)} \times 100, \tag{2.25}$$

where $R(x)$ is the dynamic radius, and $r_0(x)$ is the unstressed radius of the vessel.

3. Simulations

We use the two-step Richtmeyer Lax-Wendroff method to solve the model equations described in Sect. 2 for the large arterial and venous networks presented in Table 2. Using data from Table 2 and methods described for the structured tree model, we predict pressure, area, and flow in the large pulmonary arteries and veins. We also compute the WSS, TAWSS, and OSI for these large vessels using the boundary layer velocity profile. Using the linearized model equations to simulate the microvasculature, we predict pressure and flow along the arteriole and venule α and β branches and observe how they vary as vessel radius decreases. We also compute CS, WSS, TAWSS, and OSI in the microvasculature.

4 Results

We show results for a normotensive female adult, with network dimensions specified in Table 2. Vessel geometries and inflow into the MPA were obtained from measurements; other quantities including density and viscosity were determined from literature values (Table 1).

4.1. Normotensive case

4.1.1. Large vessels—Figures 2 and 3 show the predicted flow, pressure, and area deformation at the midpoint of the MPA, RPA, LPA, RIV, RSV, LIV, and LSV over one cardiac cycle for a healthy individual with a normotensive left atrial pressure. In the MPA, LPA, and RPA, the pressure ranges from approximately 4 mmHg to 18 mmHg. The pressure for large veins remains close to the imposed left atrial pressure with the LSV and RSV having the greatest pulse pressure over a cardiac cycle. With a cardiac output corresponding to a healthy adult, and a heartrate of 60 beats per minute, the maximum flow for the MPA, RPA, and LPA are 300 cm^3/s, 160 cm^3/s, and 100 cm^3/s, respectively. We observe that the flow decreases in each vessel as it is distributed to the downstream vasculature; however, total flow is conserved in each generation. The maximum flow rates for the LIV, LSV, RSV, and RIV are approximately 75 cm^3/s, 40 cm^3/s, 100 cm^3/s, and 50 cm^3/s, respectively. Note that since there are four veins entering the left atrium, conservation of flow dictates that the sum of the flow in these vessels equals the flow in the MPA. We also compute the cross-sectional area over a cardiac cycle for the large arteries and veins. We observe that the MPA has the largest area, ranging from approximately 5–5.6 cm^2 over a cardiac cycle. Area for the RPA ranges from 4.7 to 5.2 cm^2 and area for the LPA ranges from 4.5 to 5 cm^2. The area for the large veins does not fluctuate significantly throughout a cardiac cycle and is less than that of the arteries. Respectively, the area for the RIV, RSV, LIV, and LSV is 1.2 cm^2, 2.0 cm^2,0.8 cm^2, and 1.6 cm^2. There are small deformations in the area of these veins; however, these are not visible at the scale that the results are displayed.

We also average the wall shear stress over time (TAWSS) and display the results at the midpoint of each vessel. The TAWSS for the large arteries and veins ranges from about 8 to 3.5 $g/(cms^2)$ (Fig. 5). Vessels with smaller radii (RTA, RIA, LTA, LIA) have a higher TAWSS. We also observe that the MPA has a higher TAWSS than the RPA and LPA, Table

1 List of parameters and variables despite the latter having smaller radii. This is due to the MPA having a higher flow rate within a cardiac cycle than the RPA and LPA. The OSI is small, which indicates that the WSS is largely aligned with the TAWSS. The MPA has an OSI of approximately 0.017 and the OSI for subsequent vessels decreases throughout the arterial and venous trees. The LIV has the lowest OSI of about 0.0013 (Fig. 5).

4.1.2. Small vessels—We also predict pressure and flow in the small arteries and veins along the α and β branches (Fig. 4). In the arterioles, the pressure decreases with decreasing vessel radius with a systolic pressure of about 18 mmHg and diastolic pressure of about 2 mmHg. By contrast, in the venules, pressure increases as vessel radius increases. We set $r_{\min}$ to 0.0075 mm, ensuring that we model vessels up to the capillary level (Townsley 2012). The minimum pressure in the small veins approaches 2 mmHg at the inlet to the left atrium. For both arterioles and venules, volumetric flow rate decreases with decreasing vessel radius.

For the small vessels, shear stress is predicted along the α and β branches. In both the small arteries and veins, smaller vessel radius results in higher values for shear stress, which follows Eq. (2.22), where we observe that the shear stress is inversely proportional to the radius cubed. The β-branch has fewer vessels than the α-branch due to the asymmetric set up of the structured tree. This results in the β-branch having higher flow and shear stress, as Eq. (2.22) demonstrates the flow is proportional to shear stress (Fig. 4). For the small vessels, we plot the TAWSS with respect to vessel radius and observe that vessels with the smallest radii have the largest TAWSS at approximately $30\ \mathrm{g}/\left(\mathrm{cm}\cdot\mathrm{s}^2\right)$. This follows from the fact that vessels with smaller radii have larger WSS. The small vessels have an OSI on a scale of 10^{-3}, demonstrating that the WSS is well-aligned with the TAWSS (Fig. 5).

4.2. Isolated post-capillary pulmonary hypertension case

We simulate Ipc-PH by increasing the left atrial filling pressure from 2 to 20 mmHg and subsequently decreasing cardiac output between 10 and 100% of its normotensive value.

4.2.1. Large vessels—We observe that increasing the left atrial filling pressure propagates to the venous and arterial trees, increasing the pressure in both. The mean pressure in the large arteries becomes hypertensive when the left atrial pressure is higher than 8 mmHg (Fig. 6). The venous pressure oscillates near the imposed left atrial pressure. This is also the case for the small arteries and veins (Fig. 6). Decreasing the cardiac output contributes to a decrease in pressure for both the arteries and veins (Fig. 7).

We compute time-varying shear stress in the large arteries and veins for the Ipc-PH case (Fig. 8). For the large vessels, we compute WSS within the boundary layer at the midpoint of the MPA, RPA, and LPA, and the four large veins (LIV, LSV, RSV, RIV). The maximum shear stress through a cardiac cycle for the MPA, RPA, and LPA is $25\ \mathrm{g}/\left(\mathrm{cms}^2\right)$, $15\ \mathrm{g}/\left(\mathrm{cms}^2\right)$, and $10\ \mathrm{g}/\left(\mathrm{cms}^2\right)$. The maximum shear stress through a cardiac cycle for the RIV, RSV, LIV, and LSV is $20\ \mathrm{g}/\left(\mathrm{cms}^2\right)$, $25\ \mathrm{g}/\left(\mathrm{cms}^2\right)$, $18\ \mathrm{g}/\left(\mathrm{cms}^2\right)$, and $23\ \mathrm{g}/\left(\mathrm{cms}^2\right)$. When we increase left atrial pressure to simulate Ipc-PH, the WSS decreases in each vessel (Fig. 8). Once there is a

left atrial pressure of 20 mmHg, we decrease the cardiac output between 10 and 100% of the original inflow and observe a further decrease in WSS (Fig. 9). The shape of the WSS curve follows the volumetric flow through the cardiac cycle since shear stress is proportional to flow. In addition, the values of WSS are inversely related to the radius of the vessel (Equation 2.17). Thus, even though the arteries have larger area than the veins, the shear stress values are in similar ranges.

4.2.2. Small vessels—In the small vessels, increasing the left atrial pressure contributes to an increase in pressure for both the arteries and veins. Similar to large vessels, increasing left atrial pressure leads to decreases in WSS. We also note that CS increases with elevated left atrial pressure. CS in the small arteries with radii between 0.8 mm and r_{min} decreases from 70% to approximately 10% in the case where we impose a left atrial pressure of 20 mmHg. The venules have a Fig. 2 Predicted pressure (first row), flow (second row), and area (third row) at three locations along the large arteries, MPA (first column), RPA (second column), and LPA (third column), for left atrial pressure of 2 mmHg and typical cardiac output CS that goes from 45 to 10% (Fig. 10). We combine an elevated left atrial pressure of 20 mmHg with a reduced cardiac output. In this case, we observe that pressure and WSS decrease with decreasing cardiac output. We also note that the cyclic stretch for the arteries decreases with decreasing cardiac output. By contrast, the cyclic stretch for the venules remains the same, despite decreasing cardiac output (Fig. 11).

5 Discussion

This study is the first to develop a multiscale network model predicting WSS and CS in both large and small arteries and veins in the normotensive and Ipc-PH adult human pulmonary circulation. Our results show that the large arteries have higher pressure and flow than the large veins, as well as more pronounced changes in area throughout the cardiac cycle. In the small vessels, we see that as vessel radius decreases, pressure decreases for arterioles but increases for venules. As vessel radius decreases, we also found that the volumetric flow decreases. Simulations show that WSS, TAWSS, and OSI generally increase in both large and small vessels as radius decreases. CS decreases in arterioles as radius decreases while increasing in venules as radius decreases. When Ipc-PH is imposed through increasing the left atrial filling pressure, we observe increases in arterial and venous pressure as well as increases in CS and decreases in WSS.

Our predictions of pressure, flow, and area in the large arteries and veins agree with the literature (Qureshi et al. 2014). In the MPA, it has been shown that the systolic pressure is about 15–25 mmHg in healthy human adults with the mean pressure at about 15 mmHg. (Boron and Boulpaep 2016; Olufsen et al. 2012; Mynard and Smolich 2015; Wenger et al. 2010; Nauser and Stites 2001). The range in the value of pressure throughout the cardiac cycle agrees with Hall and Hall (2020), who reported that the mean pulmonary arterial pressure is about 16 mmHg. Our results for the normotensive case (left atrial pressure of 2 mmHg) agree with the reported lecture values for systolic and pulse pressure in the MPA. The pressure in the large veins follows the shape of predicted pressure in Qureshi et al. (2014), where the magnitude and variation in pressure remain low in the veins. The pulmonary veins have lower pressure than the arteries, which is depicted in our results and

in literature (Gao and Raj 2005). In Gao and Raj's study (2005), they determined that under different levels of perfusate hematocrit and apparent viscosity, the large pulmonary arteries have higher pressure than the large pulmonary veins.

There is a greater flow through the RPA than the LPA because the RPA has a larger radius than the LPA; however, total flow is conserved in each generation of vessels. We also note that the flow through the RSV is larger than the flow through the other veins because it is connected to the RTA, which has a larger radius (0.80 cm) than the other terminal arteries. Each of the large veins that we simulate has smaller flow than the arteries, but this is expected due to conservation of flow and the fact that there are four vessels in the generation of large veins that we observe. The smallest venules have the largest pressure, which is still less than the pressure in the arterioles. Veins have much lower pressure than arteries, which is depicted in our results and in literature (Gao and Raj 2005). Chaliki et. al measured pulmonary arterial and venous pressure in mongrel dogs and found that pulmonary venous pressure was lower than pulmonary arterial pressure but higher than left atrial pressure. This is expected due to the vein's location between the pulmonary artery and left atrium (Chaliki et al. 2002). In our model, left atrial pressure is fixed at 2 mmHg for the normotensive case; however, our results agree with that of Chaliki et al. (2002)

Several studies have used CFD models to predict WSS, TAWSS, and OSI in large pulmonary arteries (Kheyfets et al. 2015; Tang et al. 2012; Yang et al. 2019; Zambrano et al 2018). However, there has yet to be a study that investigates how local WSS changes in the entire pulmonary vasculature (Roux et al. 2020). In Yang et al. (2019), it was shown that WSS decreases in severe and moderate cases of pulmonary hypertension as compared with control individuals in the MPA, RPA, LPA, and branch PAs. PH patients usually present with a dilated MPA and maintain normotensive cardiac output before they have right ventricular failure (Yang et al. 2019). Thus, the reduction in WSS in the proximal pulmonary arteries is due to the enlargement of the MPA. We also observe a reduction in WSS when simulating Ipc-PH; however, we do not enlarge the MPA radius and instead simulate Ipc-PH by increasing left atrial pressure. In the advanced stages of PH-LHF, decreased cardiac output contributes to a reduction in WSS as well. Several MRI studies on PH patients found that the mean WSS is approximately $4 - 8\ \mathrm{g}/\left(\mathrm{cms}^2\right)$, which is similar to our TAWSS values in the large vessels (Truong et al. 2013; Schäfer et al. 2017). As the disease progressed, they observed that the values of WSS climbed in the arterial tree toward the proximal vessels, suggesting a link between WSS and vascular remodeling in PH, which is known to begin in the small arteries and spread to larger arteries as the disease progresses (Postles et al. 2014). Due to challenges of imaging and measuring flow in the distal pulmonary vasculature, less is known about WSS in the downstream vasculature, and computational approximations are relied upon to make predictions. Since WSS is inversely proportional to the vessel radius cubed, WSS increases significantly as the vessel radius decreases. Our results show that WSS increases in the microcirculation agreeing with recent findings reported in literature (Yang et al. 2019; Kheyfets et al. 2015; Postles et al. 2014; Ghorishi et al. 2007; Allen et al. 2014). The results presented in Kheyfets et al. (2015) and Yang et al. (2019) show that, in general, WSS continues to increase for vessels in the downstream vasculature that have smaller vessels. More specifically, Yang et al. show that

WSS in the distal PAs increased significantly with decreasing vessel radius and that mean WSS for segments between 100 and 500 μm increased to as much as 116 $g/(cms^2)$. Although we model vessels up to a radius of 7.5 μm, our WSS predictions follow their results, and our WSS values go up to 100 $g/(cms^2)$ in our smallest vessels. In addition, results from Kheyfits et al. indicate that WSS increases drastically in vessels with smaller diameter. Even though they bound their WSS calculations to 50 $g/(cms^2)$, they demonstrate that WSS is lowest in the MPA and increases as flow propagates down the arterial tree (Kheyfets et al. 2015). Other mathematical models of the pulmonary vasculature reported high values of shear stress in human and animal PH simulations, varying between approximately 160 and 1000 $g/(cms^2)$ depending on the model assumptions and geometry (Postles et al. 2014; Ghorishi et al. 2007; Allen et al. 2014). This increase in WSS in the microvasculature is due to a reduction in cross-sectional area requiring more energy to transport the same amount of flow through fewer and narrower vessels per unit time. In addition, we have that the β-branch has fewer vessels than the α-branch with the same flow enforced. We see that this leads to the β-branch displaying higher WSS, which aligns with observations made in Yang et al. (2019).

It is important to note that our results for WSS and TAWSS are based on geometry from CT images with specified inflow profile based on data in the large vessels, whereas predictions made in the microvasculature are approximations based on a structured tree. Therefore, the use of the structured tree model should be considered an estimation based on our model assumptions, rather than a patient specific evaluation. Different mathematical models will yield varying results; however, the general idea that WSS increases in the distal vasculature and decreases with elevated left atrial pressure holds. In addition, it has been observed that WSS derived from an MRI are generally lower than WSS found from CFD.

Many prior studies calculate WSS, TAWSS, and OSI using 3D simulations, but here we use a 1D model to make predictions. In Zambrano et al. (2018), it was reported that TAWSS values are higher in the third generation of the pulmonary arteries as opposed to the first and second generations (Zambrano et al. 2018). Although our results are not identical to those reported by Zambrano et al. our TAWSS values follow the same pattern; they increase as vessel radius decreases, and in the smallest vessels, Zambrano et al. report a WSS value of 30 $g/(cms^2)$, which agrees with our findings in the large vessels. They also show that PH patients have a reduction in TAWSS, consistent with our results. The noted discrepancies between our study and Zambrano are due to a difference in mathematical model used and shear stress calculation. WSS can be calculated relative to undeformed or deformed radius, which can significantly change values obtained. Our OSI is very small, indicating that the WSS is largely aligned with the TAWSS. The MPA has an OSI of approximately 0.017, and the OSI for subsequent vessels decreases throughout the arterial and venous trees. The LIV has the lowest OSI of about 0.0013. The OSI for arterioles and venules are on the scale of 10^{-3}. These values are lower than reports from Zambrano and Yang; however, the values follow a similar pattern of decreasing with decreased vessel radius and increasing with PH-LHF. OSI were reported with the normalized distance in MPA, RPA, and LPA and throughout the three-dimensional vessels, and we report the value at the midpoint of our 1D vessels, which may contribute to the discrepancies that we observe. Discrepancies may

also be due to data acquisition, geometry, mathematical model used, and the fact that other studies did not investigate these quantities in arterioles or venules.

To our knowledge, no previous studies have calculated CS in the arterioles and venules using a CFD model. In the context of our assumptions, our results demonstrate that arterioles have a larger change in CS as radius decreases than venules. The vessels with smaller radius have smaller CS due to the increase in stiffness as radius decreases (Equation 2.8). Although pulmonary veins have higher compliance than pulmonary arteries (Boron and Boulpaep 2016), the change in pressure over a cardiac cycle for the veins is smaller. Thus, the radii of the veins change less significantly, resulting in smaller CS. Our results for venous CS are physiologically too high because we do not model the capillaries, where dampening occurs.

Arteries and veins are composed of the same material (elastin and collagen), and it is known that their material properties differ from vessels in the systemic vasculature as smooth muscle cells surround both small arteries and veins (Townsley 2012). Several studies have reported that pulmonary veins are stiffer than the pulmonary arteries (Banks et al. 1978; Wiener et al. 1966) and even though Krenz and Dawson (2003) note that the vessel stiffness is constant across scale, several newer studies (Townsley 2012; Stack et al. 2014; Sicard et al. 2017) have found that vessels in the microvasculature are stiffer than the large vessels. Therefore, we chose to let small vessel stiffness Eh/r_0 increase with decreasing radius. Moreover, to ensure smooth transition in vessel stiffness from large to small vessels, values for k_1 and k_3 are set such that vessel stiffness is the same in the terminal large vessel and the root vessel of the structured tree. The model parameters used to predict vessel stiffness are chosen to provide appropriate qualitative behavior, but more work is needed to identify appropriate parameter ranges for both large and small pulmonary arteries and veins.

We impose a higher stiffness in the venules, which causes a smaller deformation over a cardiac cycle. Krenz and Dawson (2003) demonstrated that the pulmonary wall structure varies considerably from the MPA to the precapillary arteries, but noted that distensibility remains constant independent of vascular diameter and vessel wall composition.

5.1. Future developments and limitations

In the present study, we utilized a 1D CFD model that connects large arteries and veins with geometry from segmented images to small vessels represented by structured trees. We study conditions that correspond to a healthy adult with a inflow profile that has a normotensive cardiac output and left atrial pressure of 2 mmHg. We also elevate the left atrial filling pressure, ranging from 2 to 20 mmHg, and decrease cardiac output in order to simulate Ipc-PH. We plan to further develop this study by including additional conditions that correspond to Cpc-PH, which is associated with remodeling of the vasculature. Increased venous stiffness may contribute to Ipc-PH; however, our simulations with increasing stiffness did not yield significant qualitative differences, so we chose to omit this. Eslami et al. (2020) used a 3D model to study WSS and deduced that flexible walls don’t change the results when compared to completely rigid walls. We plan to further analyze the impact of vessel elasticity on our model, but believe that our results are reasonable when compared to Eslami et al. (2020). Overall, analyzing results that correspond to disease progression will allow us to further understand the mechanisms involved in PH-LHF progression.

Another limitation of this study is that we neglect the pulmonary capillaries. Currently, flow in the smallest arterioles, venules, and capillaries (vessels with radius less than 7.5 μm) are not modeled. It has been shown that blood flow through the capillaries resembles a sheet due to its dense and irregular pattern, making a structured tree model unsuitable to simulate these regions. Future studies will combine three models: large arteries and veins with geometry from segmented images, small vessels represented by structured trees, and capillaries represented by a sheet model (Fung and Sobin 1969).

We also do not account for the gravitational gradient that impacts hemodynamics in the veins. Differences in hydrostatic pressures impact distensibility of vessels, vascular resistance, and blood flow (Wieslander et al. 2019). Because pulmonary veins lack smooth muscle, the vessel wall compliance can be expected to be high and hence, blood volume in the veins are sensitive to pressure changes caused by the effects of gravity (Wieslander et al. 2019).

This study uses a 1D network model for predictions. Several studies have compared pressure and flow predictions between 1D and 3D models (Blanco et al. 2018), but to our knowledge, none of these studies compared 1D and 3D shear stress predictions. Adding a 3D model is beyond the scope of this study, but future studies will aim to compare 1D and 3D shear stress predictions in the pulmonary vasculature. Results may be of importance in regions with significant secondary flows, for example in curved vessels and in junctions. 3D computations may allow us to examine if 3D predictions are needed at all, in both large and small vessels, or only in the large vessels. Finally, while such simulations could be important, it should be noted that differences between subjects are likely greater than what is gained by adding detailed 3D predictions.

5.2. Conclusion

The in-silico computational fluid dynamics model presented in this study is an important tool that provides a new way to analyze and investigate hypotheses related to understanding the physiological mechanisms underlying the progression of pulmonary vascular diseases. We predict WSS and CS in the large and small pulmonary arteries and veins, as these quantities are believed to alter mechanical forces, which in turn impact PH-LHF progression. We study pulmonary hemodynamics in a physiologically healthy individual as well as one with Ipc-PH and find that WSS decreases and CS increases in the presence of disease, confirming a link between these quantities and remodeling. Prior to this study, these forces had not yet been quantitatively defined in the complete pulmonary vasculature for a healthy subject and PH-LHF patient. Our results for a physiologically healthy subject agree with previous studies, while also providing quantitative measurements for values not previously predicted.

Acknowledgements

This work was supported in part by the National Institute of Health (NIH-HLBI 5R01HL147590–02 and NIH-NIAID 1R01AI139085–01), the National Science Foundation (NSF-DMS 1615820) and the American Heart Association (AHA 19PRE34380459).

Appendix

As described in detail by Qureshi et al. (2014), for the arterial and venous networks we define a relation between pressure and flow at both ends of each vessel, and derive a boundary condition that matches pressure and flow at the terminal large arteries and veins. To do so, we compute the admittance of each structured tree, relating pressure and flow at the outlet of each large terminal artery to pressure and flow at the inlet to the corresponding large terminal vein. At each junction, we set up an admittance matrix satisfying continuity of pressure and conservation of volume flux. The total admittance is calculated by joining "junction" admittances in series and parallel as illustrated in Fig. 12.

Given the proximal and distal flow $Q_1 = Q(0,\omega)$ and $Q_2 = Q(L,\omega)$, the admittance matrix is obtained by relating the flow and pressure at the proximal, $x = 0$, and distal, $x = L$, ends of a vessel of radius r_0 yielding

$$\begin{pmatrix} Q_1 \\ Q_2 \end{pmatrix} = \frac{ig_\omega}{S_L}\begin{pmatrix} -C_L & 1 \\ 1 & -C_L \end{pmatrix}\begin{pmatrix} P_1 \\ P_2 \end{pmatrix} \tag{6.1}$$

where $C_L \equiv \cos(\omega L/c)$, $S_L \equiv \sin(\omega L/c)$, and

$$\mathbf{Y}(\omega) = \frac{ig_\omega}{S_L}\begin{pmatrix} -C_L & 1 \\ 1 & -C_L \end{pmatrix} \tag{6.2}$$

is the admittance matrix for any one artery or vein when $\omega \neq 0$. For $\omega = 0$,, we have

$$\begin{pmatrix} Q_1 \\ Q_2 \end{pmatrix} = \frac{\pi r^4}{8\mu L}\begin{pmatrix} 1 & -1 \\ -1 & 1 \end{pmatrix}\begin{pmatrix} P_1 \\ P_2 \end{pmatrix}. \tag{6.3}$$

and therefore

$$\mathbf{Y}(0) = \frac{\pi r^4}{8\mu L}\begin{pmatrix} 1 & -1 \\ -1 & 1 \end{pmatrix}. \tag{6.4}$$

For two vessels (S and T) in parallel, continuity of pressure between the inlet and outlet and conservation of volume flux across the junction gives

$$\begin{pmatrix} Q_1 \\ Q_2 \end{pmatrix} = \mathbf{Y}^{\parallel}\begin{pmatrix} P_1 \\ P_2 \end{pmatrix}, \tag{6.5}$$

where Q_1 and Q_2 denote the vessel inflow and outflow, P_1 and P_2 are the corresponding inlet and outlet pressure, and $\mathbf{Y}^{\parallel} = \mathbf{Y}^S + \mathbf{Y}^T$. We denote $\mathbf{Y}^S$ and $\mathbf{Y}^T$ as the admittances for vessel S and T, respectively.

Similarly, for two vessels (S and T) connected in series flow and pressure are related by

$$Q_k^i = \sum_{l=1}^{2} Y_{kl}^i P_l^i \tag{6.6}$$

where $i = S, T$ and $k = 1,2$ with Y_{kl} being the components of the 2×2 admittance matrix. Assuming that $P = P_2^S = P_1^T$ and $Q_2^S = -Q_1^T$ at the junction of two vessels in series, the system for the vessels is represented by

$$\begin{pmatrix} Q_1^S \\ Q_2^T \end{pmatrix} = \mathbf{Y}^{\Leftrightarrow} \begin{pmatrix} P_1^S \\ P_2^T \end{pmatrix} \tag{6.7}$$

where

$$\mathbf{Y}^{\Leftrightarrow} = \frac{1}{Y_{22}^S + Y_{11}^T} \times \begin{pmatrix} \det\left(\mathbf{Y}^S\right) + Y_{11}^S Y_{11}^T & -Y_{12}^S Y_{12}^T \\ -Y_{21}^S Y_{21}^T & \det\left(\mathbf{Y}^T\right) + Y_{22}^S Y_{22}^T \end{pmatrix} \tag{6.8}$$

is the admittance matrix. The symbol ⇔ denotes that the vessels are joined in series.

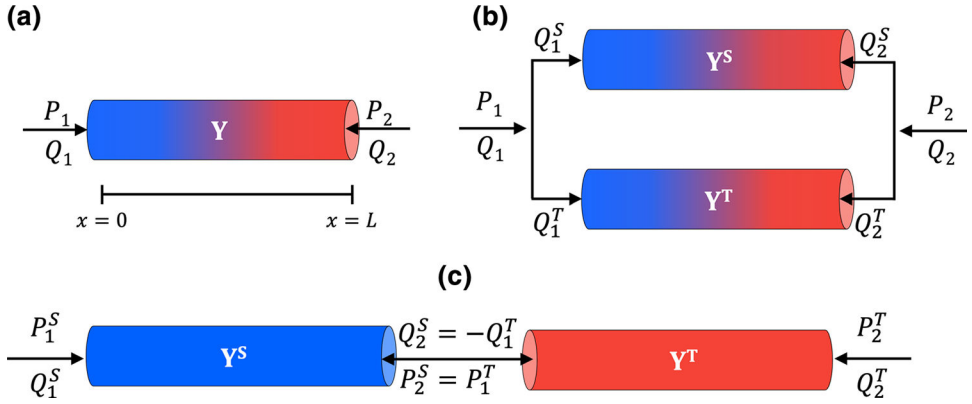

Fig. 12.

Relationship between flow and pressure via admittance $\mathbf{Y}$, $\mathbf{Y}^{\|}$ and $\mathbf{Y}$ ⇔ for a single vessel (**a**), vessels connected in parallel (**b**), and vessels connected in series (**c**). Note that $\mathbf{Y}$ is the admittance for a single vessel, $\mathbf{Y}^S$ is the admittance for vessel S, and $\mathbf{Y}^S$ is the admittance for vessel T. Here, the color blue represents deoxygenated arteries, and red represents oxygen-rich veins is the admittance matrix. The symbol ⇔ denotes that the vessels are joined in series.

To compute pressure and flow in the arterioles and venules, we first prescribe the pressure from the terminal large arteries or veins at the start of the structured tree, i.e. $P^A(0,\omega)$ and $P^V(0,\omega)$. The corresponding flows are calculated using the grand admittance,

$$Q^A(0,\omega) = Y_{11}P^A(0,\omega) + Y_{12}P^V(0,\omega),$$

$$Q^V(0,\omega) = Y_{21}P^A(0,\omega) + Y_{22}P^V(0,\omega).$$

The small vessel pressure and flow at $x = L$ are determined by

$$P^j(L,\omega) = P^j(0,\omega)C_L - \frac{iS_L}{g_\omega}Q^j(0,\omega), \tag{6.9}$$

$$Q^j(L,\omega) = \frac{ig_\omega}{S_L}\left(P^j(0,\omega) - C_L P^j(L,\omega)\right) \tag{6.10}$$

for $j = A, V$ and $\omega \neq 0$, whereas the zeroth frequency solutions are

$$P^j(L,\omega) = P^j(0,\omega) - \frac{8\mu L}{\pi r^4}Q^j(0,\omega), \tag{6.11}$$

$$Q^j(L,\omega) = \frac{\pi r^4}{8\mu L}\left(P^j(0,\omega) - P^j(L,\omega)\right). \tag{6.12}$$

References

Allen B, van Ooij P, Barker A, Collins J, Carr J, Markl M, Kansal P (2014) Impact of beta-blocker therapy on thoracic aorta 3d wall shear stress in patients with bicuspid aortic valve. J Cardiovasc Magn Reson 16:1–2 [PubMed: 24387349]

Antiga L, Piccinelli M, Botti L, EIordache B, Remuzzi A, Steinman D (2008) An image-based modeling framework for patient-specific computational hemodynamics. Med Biol Eng Comput 46:1097 [PubMed: 19002516]

Banks J, Booth FM, MacKay E, Rajagopalan B, De J, Lee G (1978) The physical properties of human pulmonary arteries and veins. Clin Sci Mol Med 55:477–484 [PubMed: 720001]

Barron V, Brougham C, Coghlan K, McLucas E, OMahoney D, Stenson-Cox C, McHugh P (2007) The effect of physiological cyclic stretch on the cell morphology, cell orientation and protein expression of endothelial cells. J Mater Sci Mat Med 18:1973–1981

Birukov K (2009) Cyclic stretch, reactive oxygen species, and vascular remodeling. Antioxi Redox Signal 11:1651–1667

Blanco P, Bulant C, Müller L, Talou G, Bezerra C, Lemos P, Feijóo R (2018) Comparison of 1d and 3d models for the estimation of fractional flow reserve. Sci Rep 8:1–12 [PubMed: 29311619]

Blanco P, Feijóo R (2010) A 3d–1d-0d computational model for the entire cardiovascular system. Mecánica Comput 29:5887–5911

Boron W, Boulpaep E (2016) Medical physiology E-book. Elsevier Health Sciences, Amsterdam

Caro C, Saffman P (1965) Extensibility of blood vessels in isolated rabbit lungs. J Physiol 178:193–201 [PubMed: 14298115]

Chaliki H, Hurrell D, Nishimura R, Reinke R, Appleton C (2002) Pulmonary venous pressure: relationship to pulmonary artery, pulmonary wedge, and left atrial pressure in normal, lightly sedated dogs. Catheter Cardiovasc Interv 56:432–438 [PubMed: 12112902]

Chambers M, Colebank M, Qureshi M, Clipp R, Olufsen M (2020) Structural and hemodynamic properties of murine arterial networks under hypoxia-induced pulmonary hypertension. Proc Inst Mech Eng Part H: J Eng Med p. 0954411920944110

Chambers M, Colebank M, Qureshi M, Clipp R, Olufsen M (2020) Structural and hemodynamic properties of murine pulmonary arterial networks under hypoxia-induced pulmonary hypertension. Proc Inst Mech Eng Part H J Eng Med 234:1312–1329

Clark A, Tawhai M (2018) Temporal and spatial heterogeneity in pulmonary perfusion: a mathematical model to predict interactions between macro-and micro-vessels in health and disease. The ANZIAM J 59:562–580

Colebank M, Paun L, Qureshi M, Chesler N, Husmeier D, Olufsen M, Fix L (2019) Influence of image segmentation on one-dimensional fluid dynamics predictions in the mouse pulmonary arteries. J Royal Soc Interf 16:20190,284

Colebank M, Qureshi M, Rajagopal S, Krasuski R, Olufsen M (2021) A multiscale model of vascular function in chronic thromboembolic pulmonary hypertension. Am J Physiol. 10.1152/ajpheart.00086.2021

Davies P (2009) Hemodynamic shear stress and the endothelium in cardiovascular pathophysiology. Nature Clin Prac Cardiovasc Med 6:16–26

Eslami P, Tran J, Jin Z, Karady J, Sotoodeh R, Lu M, Hoffmann U, Marsden A (2020) Effect of wall elasticity on hemodynamics and wall shear stress in patient-specific simulations in the coronary arteries. J Biomech Eng 142:024503 [PubMed: 31074768]

Fung Y, Sobin S (1969) Theory of sheet flow in lung alveoli. J Appl Physiol 26:472–488 [PubMed: 5775333]

Gao Y, Raj J (2005) Role of veins in regulation of pulmonary circulation. Am J Physiol 288:L213–L226

Gerges M, Gerges C, Pistritto A, Lang M, Trip P, Jakowitsch J, Binder T, Lang I (2015) Pulmonary hypertension in heart failure. epidemiology, right ventricular function, and survival. Am J Respir Crit Care 192:1234–1246

Ghio S, Gavazzi A, Campana C, Inserra C, Klersy C, Sebastiani R, Arbustini E, Recusani F, Tavazzi L (2001) Independent and additive prognostic value of right ventricular systolic function and pulmonary artery pressure in patients with chronic heart failure. J Am Coll Cardiol 37:183–188 [PubMed: 11153735]

Ghorishi Z, Milstein J, Poulain F, Moon-Grady A, Tacy T, Bennett S, Fineman J, Eldridge M (2007) Shear stress paradigm for perinatal fractal arterial network remodeling in lambs with pulmonary hypertension and increased pulmonary blood flow. Am J Physiol 292:H3006–H3018

Guazzi M, Borlaug B (2012) Pulmonary hypertension due to left heart disease. Circulation 126:975–990 [PubMed: 22908015]

Guglin M, Khan H (2010) Pulmonary hypertension in heart failure. J Card Fail 16:461–474 [PubMed: 20610227]

Hall J, Hall M (2020) Guyton and Hall textbook of medical physiology e-Book. Elsevier Health Sciences, Amsterdam

He X, Ku D (1996) Pulsatile flow in the human left coronary artery bifurcation: average conditions. J Bomech Eng 118:74–82

Huang W, Yen R, McLaurine M, Bledsoe G (1996) Morphometry of the human pulmonary vasculature. J Appl Physiol 81:2123–2133 [PubMed: 8941537]

Kheyfets V, Rios L, Smith T, Schroeder T, Mueller J, Murali S, Lasorda D, Zikos A, Spotti J, Reilly JJ, Finol E (2015) Patient-specific computational modeling of blood flow in the pulmonary arterial circulation. Comp Meth Prog Biomed 120:88–101

Krenz GS, Dawson CA (2003) Flow and pressure distributions in vascular networks consisting of distensible vessels. Am J Physiol 284:H2192–H2203

Lam C, Roger V, Rodeheffer R, Borlaug B, Enders F, Redfield M (2009) Pulmonary hypertension in heart failure with preserved ejection fraction: a community-based stud. J Am Coll Cardiol 53:1119–1126 [PubMed: 19324256]

Lighthill SJ (1975) Mathematical biofluiddynamics. SIAM, Philadelphia, PA

Maloney J, Rooholamini S, Wexler L (1970) Pressure-diameter relations of small blood vessels in isolated dog lung. Microvasc Res 2:1–12 [PubMed: 5523912]

Michel T, Paul MV (2010) Cellular signaling and no production. Eur J Physiol 459:807–816

Miller W, Grill D, Borlaug B (2013) Clinical features, hemodynamics, and outcomes of pulmonary hypertension due to chronic heart failure with reduced ejection fraction: pulmonary hypertension and heart failure. JACC Heart Fail 1:290–299 [PubMed: 24621932]

Moraes D, Loscalzo J (1997) Pulmonary hypertension: newer concepts in diagnosis and management. Clin Cardiol 20:676–682 [PubMed: 9259160]

Mozaffarian D, Benjamin E, Go A, Arnett D, Blaha M, Cushman M, Das S, de Ferranti S, Despres J, Fullerton H, Howard V, Huffman M, Isasi C, Jimenez M, Judd S, Kissela B, Lichtman J, Lisabeth L, Liu S, Mackey R, Magid D, McGuire D, Mohler ER, Moy C, Muntner P, Mussolino M, Nasir K, Neumar R, Nichol G, Palaniappan L, Pandey D, Reeves M, Rodriguez C, Rosamond W, Sorlie P, Stein J, Towfighi A, Turan T, Virani S, Woo D, Yeh R, Turner M, Members WG, Committee AHAS, Subcommittee SS (2016) Heart disease and stroke statistics-2016 update: a report from the american heart association. Circulation 133:e38–e360. 10.1161/CIR.0000000000000350 [PubMed: 26673558]

Mynard J, Smolich J (2015) One-dimensional haemodynamic modeling and wave dynamics in the entire adult circulation. Ann Biomed Eng 43:1443–1460 [PubMed: 25832485]

Nauser TD, Stites SW (2001) Diagnosis and treatment of pulmonary hypertension. Am Fam Phys 63:1789

Nichols W, ORourke M, Kenney W (1991) Mcdonalds blood flow in arteries: theoretical, experimental and clinical principles

Olufsen M, Hill N, Vaughan G, Sainsbury C, Johnson M (2012) Rarefaction and blood pressure in systemic and pulmonary arteries. J Fluid Mech 705:280–305 [PubMed: 22962497]

Olufsen M, Peskin C, Kim W, Pedersen E, Nadim A, Larsen J (2000) Numerical simulation and experimental validation of blood flow in arteries with structured-tree outflow conditions. Ann Biomed Eng 28:1281–1299 [PubMed: 11212947]

Papadaki M, Mclntire L (1999) Quantitative measurement of shear-stress effects on endothelial cells. In: Tissue Engineering Methods and Protocols, pp. 577–593. Springer

Paszkowiak J, Dardik A (2003) Arterial wall shear stress: observations from the bench to the bedside. Vasc Endovasc Surg 37:47–57

Paun L, Colebank M, Olufsen M, Hill N, Husmeier D (2020) Assessing model mismatch and model selection in a bayesian uncertainty quantification analysis of a fluid-dynamics model of pulmonary blood circulation. J Royal Soc Interf 17:20200,886

Pedersen E (1993) In vitro and in vivo studies of blood flow in the normal abdominal aorta and aorta bifurcation. Tech. rep., Technical Report, Århus University Hospital, Skejby, Denmark

Pedersen E, Sung HW, Burlson A, Yoganathan A (1993) Two-dimensional velocity measurements in a pulsatile flow model of the normal abdominal aorta simulating different hemodynamic conditions. J Biomech 26:1237–1247 [PubMed: 8253828]

Postles A, Clark A, Tawhai M (2014) Dynamic blood flow and wall shear stress in pulmonary hypertensive disease. In: 2014 36th Ann Int Conf of the IEEE Eng Med Biol Soc, pp. 5671–5674. IEEE

Pries A, Neuhaus D, Gaehtgens P (1992) Blood viscosity in tube flow: dependence on diameter and hematocrit. Am J Physiol 263:H1770–H1778 [PubMed: 1481902]

Qureshi M, Vaughan G, Sainsbury C, Johnson M, Peskin C, Olufsen M, Hill N (2014) Numerical simulation of blood flow and pressure drop in the pulmonary arterial and venous circulation. Biomech Model Mechanobiol 13:1137–1154 [PubMed: 24610385]

Ramu B, Thenappan T (2016) Evolving concepts of pulmonary hypertension secondary to left heart disease. Curr Heart Fail Rep 13:92–102 [PubMed: 26886381]

Ravi Y, Selvendiran K, Naidu S, Meduru S, Citro L, Bognar B, Khan M, Kalai T, Hideg K, Kuppusamy P, Sai-Sudhakar C (2013) Pulmonary hypertension secondary to left-heart failure involves peroxynitrite-induced downregulation of pten in the lung. Hypertension 61:593–601 [PubMed: 23339168]

Reymond P, Bohraus Y, Perren F, Lazeyras F, Stergiopulos N (2011) Validation of a patient-specific one-dimensional model of the systemic arterial tree. Am J Phsyiol 301:H1173–H1182

Reymond P, Perren F, Lazeyras F, Stergiopulos N (2012) Patient-specific mean pressure drop in the systemic arterial tree, a comparison between 1-d and 3-d models. J Biomech 45:2499–2505 [PubMed: 22884968]

Riches A, Sharp J, Thomas DB, Smith SV (1973) Blood volume determination in the mouse. J Physiol 228:279–284 [PubMed: 4687099]

Roux E, Bougaran P, Dufourcq P, Couffinhal T (2020) Fluid shear stress sensing by the endothelial layer. Front Physiol 11:861 [PubMed: 32848833]

Schäfer M, Ivy D, Barker A, Kheyfets V, Shandas R, Abman S, Hunter K, Truong U (2017) Characterization of cmr-derived haemodynamic data in children with pulmonary arterial hypertension. Eur Heart J Cardiovasc Imag 18:424–431

Segers P, Dubois F, De Wachter D, Verdonck P (1998) Role and relevancy of a cardiovascular simulator. Cardiovasc Eng 3:48–56

Selzer A (1992) Understanding heart disease. University of California Press, Berkeley, CA

Sicard D, Fredenburgh L, Tschumperlin D (2017) Measured pulmonary arterial tissue stiffness is highly sensitive to afm indenter dimensions. J Mech Behavior Biomed Mater 74:118–127

Simonneau G, Montani D, Celermajer D, Denton C, Gatzoulis M, Krowka M, Williams P, Souza R (2019) Haemodynamic definitions and updated clinical classification of pulmonary hypertension. Eur Respir J 53:1801,913

Sobin S, Lindal R, Bernick S (1977) The pulmonary arteriole. Microvasc Res 14:227–239 [PubMed: 927220]

Spilker R, Feinstein J, Parker D, Reddy V, Taylor C (2007) Morphometry-based impedance boundary conditions for patient-specific modeling of blood flow in pulmonary arteries. Ann Biomed Eng 35:546–559 [PubMed: 17294117]

Stack A, Derksen F, Williams K, Robinson N, Jackson W (2014) Lung region and racing affect mechanical properties of equine pulmonary microvasculature. J Appl Physiol 117:370–376 [PubMed: 24925981]

Stalder A, Russe M, Frydrychowicz A, Bock J, Hennig J, Markl M (2008) Quantitative 2d and 3d phase contrast mri: optimized analysis of blood flow and vessel wall parameters. Magnetic Reson Med 60:1218–1231

Stergiopulos N, Young D, Rogge T (1992) Computer simulation of arterial flow with applications to arterial and aortic stenoses. J Biomech 25:1477–1488 [PubMed: 1491023]

Tang B, Fonte T, Chan F, Tsao P, Feinstein J, Taylor C (2011) Three-dimensional hemodynamics in the human pulmonary arteries under resting and exercise conditions. Ann Biomed Eng 39:347–358 [PubMed: 20640512]

Tang B, Pickard S, Chan F, Tsao P, Taylor C, Feinstein J (2012) Wall shear stress is decreased in the pulmonary arteries of patients with pulmonary arterial hypertension: an image-based, computational fluid dynamics study. Pulm Circ 2:470–476 [PubMed: 23372931]

Townsley M (2012) Structure and composition of pulmonary arteries, capillaries and veins. Comprehen Physiol 2:675

Truong U, Fonseca B, Dunning J, Burgett S, Lanning C, Ivy D, Shandas R, Hunter K, Barker A (2013) Wall shear stress measured by phase contrast cardiovascular magnetic resonance in children and adolescents with pulmonary arterial hypertension. J Cardiovasc Magn Reson 15:1–9 [PubMed: 23324167]

van Duin R, Stam K, Cai Z, Uitterdijk A, Garcia-Alvarez A, Ibanez B, Danser A, Reiss I, Duncker D, Merkus D (2019) Transition from post-capillary pulmonary hypertension to combined pre-and post-capillary pulmonary hypertension in swine: a key role for endothelin. J Physiol 597:1157–1173 [PubMed: 29799120]

Van de Vosse F, Stergiopulos N (2011) Pulse wave propagation in the arterial tree. Ann Rev Fluid Mech 43:467–499

Wenger N, Boden W, Carabello B, Carney R, Cerqueira M, Criqul M (2010) Cardiovascular disability: updating the social security listings. Nat Acad Sci

Westerhof N, Bosman F, De Vries C, Noordergraaf A (1969) Analog studies of the human systemic arterial tree. J Biomech 2:121–143 [PubMed: 16335097]

Wiener F, Morkin E, Skalak R, Fishman A (1966) Wave propagation in the pulmonary circulation. Circ Res 19:834–850 [PubMed: 5917852]

Wieslander B, Ramos J, Ax M, Petersson J, Ugander M (2019) Supine, prone, right and left gravitational effects on human pulmonary circulation. J Cardiovasc Magn Reson 21:1–15 [PubMed: 30612574]

Wilson N, Ortiz A, Johnson A (2013) The vascular model repository: a public resource of medical imaging data and blood flow simulation results. J Med Dev 7:040923

Yang W, Dong M, Rabinovitch M, Chan FP, Marsden A, Feinstein J (2019) Evolution of hemodynamic forces in the pulmonary tree with progressively worsening pulmonary arterial hypertension in pediatric patients. Biomech Model Mechanobiol 18:779–796 [PubMed: 30635853]

Yen R, Foppiano L (1981) Elasticity of small pulmonary veins in the cat. J Biomech Eng 103:38–42 [PubMed: 7253611]

Zambrano B, McLean N, Zhao X, Tan JL, Zhong L, Figueroa C, Lee L, Baek S (2018) Image-based computational assessment of vascular wall mechanics and hemodynamics in pulmonary arterial hypertension patients. J Biomech 68:84–92 [PubMed: 29310945]

Zamir M, Budwig R (2002) Physics of pulsatile flow. Appl Mech Rev 55:B35–B35

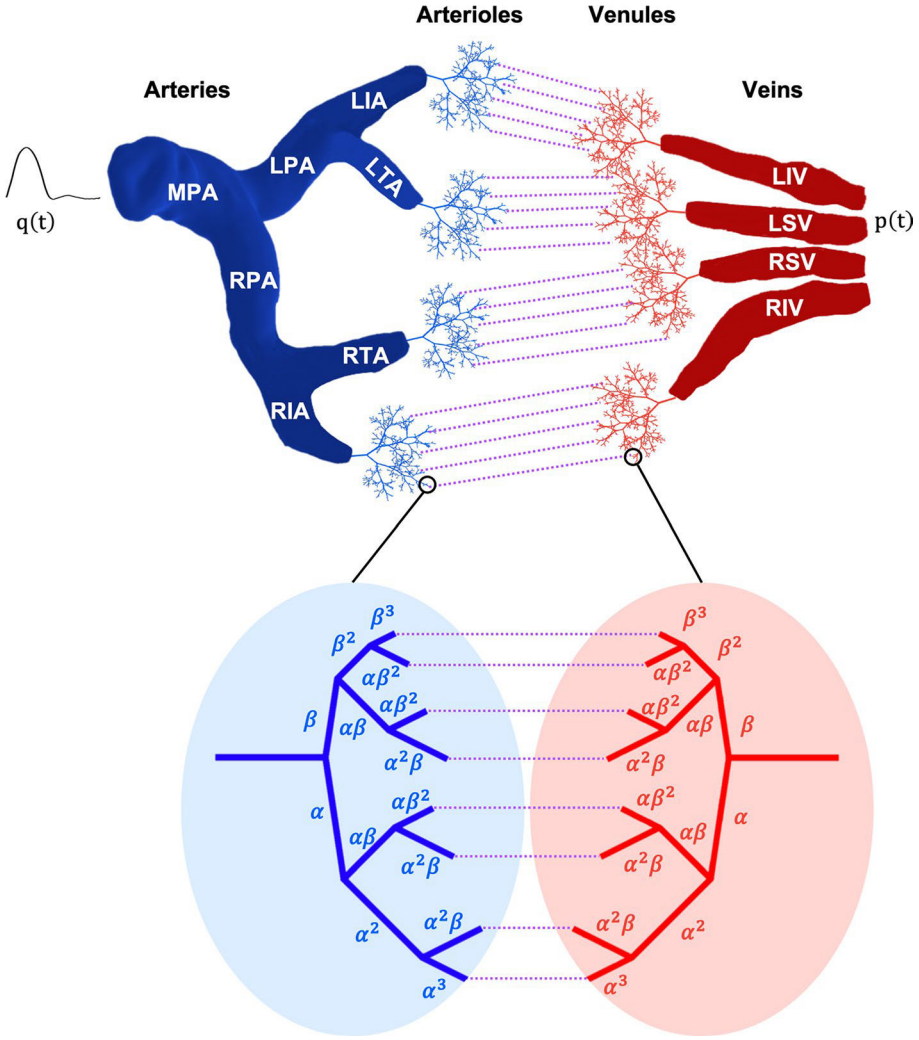

Fig. 1.

Schematic of the pulmonary circulation arranged in order of large arteries, arterioles, venules, and large veins. The dotted purple line represents the capillary beds which are not included in our model. The large arteries and veins are modeled explicitly using a CT image from a healthy human adult, and the small vessels are modeled using a structured tree. In the structured tree, each small artery has a mirroring vein. The asymmetry of the structured tree is determined by the scaling factors, α and β. We impose an inflow profile at the MPA as well as a left atrial pressure of 2 mmHg at the pulmonary veins

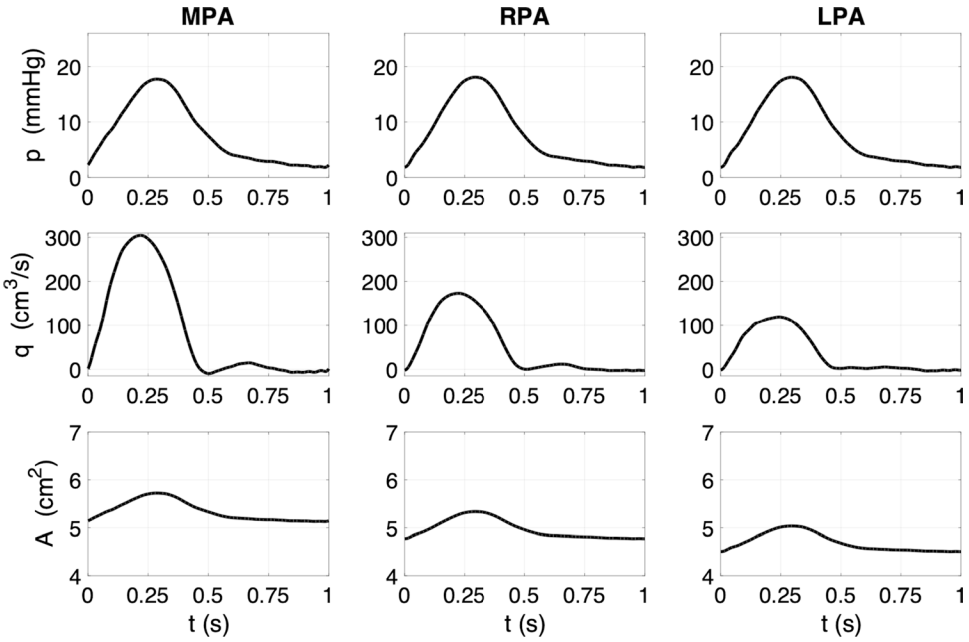

Fig. 2.

Predicted pressure (frst row), fow (second row), and area (third row) at three locations along the large arteries, MPA (frst column), RPA (second column), and LPA (third column), for left atrial pressure of 2 mmHg and typical cardiac output

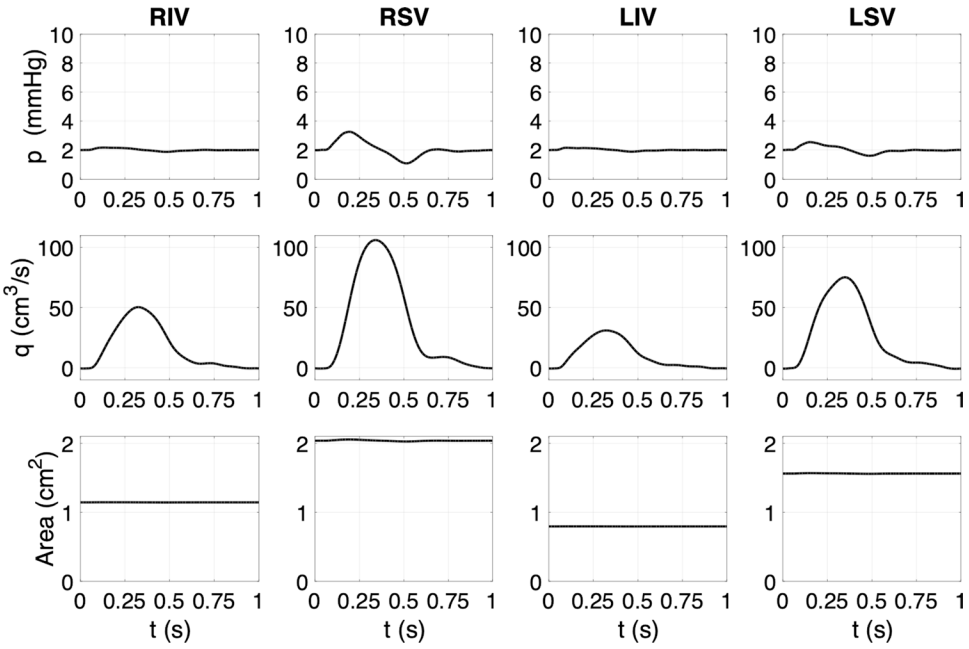

Fig. 3.

Predicted pressure (first row), flow (second row), and area (third row) at the four large pulmonary veins, LIV (first column), LSV (second column), RSV (third column), and RIV (fourth column) for left atrial pressure of 2 mmHg and typical cardiac output

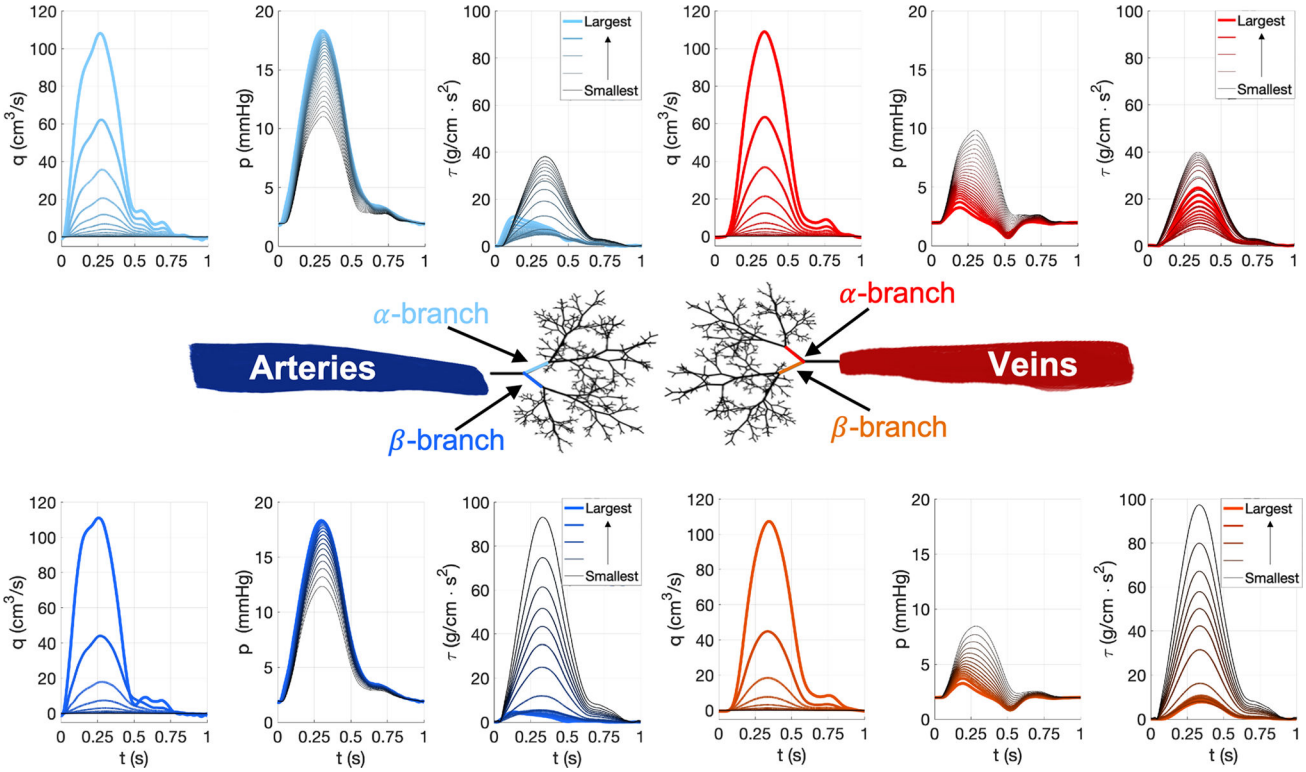

Fig. 4.

Predicted flows, pressure, and WSS for small arteries and veins along the α and β branches of the structured tree. Arteries are shown in the first column, and veins are shown in the second column smallest vessels are represented by thin black lines with results for the α branch shown in the top row and results for the β branch shown in the bottom row. The largest vessels are represented by colored thick lines and as we move down the structured tree, the smallest vessels are represented by thin black lines

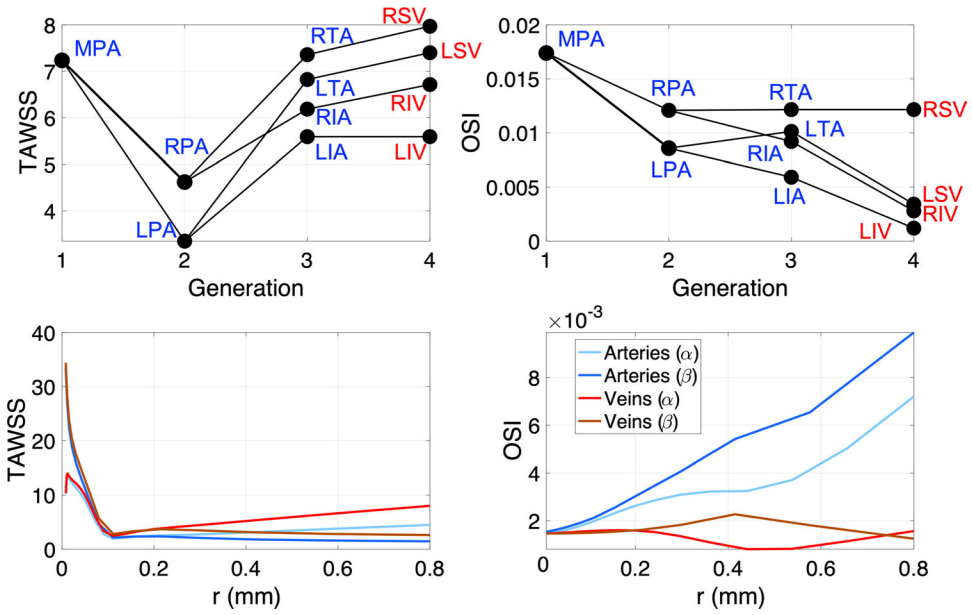

Fig. 5.

Time averaged wall shear stress (TAWSS) and oscillatory shear index (OSI) predictions for large and small arteries. Results for the large vessels are shown in the top row. Here, nodes represent the midpoint of the vessel, length of the edges represent distance between the midpoints of successive vessels, and terminal nodes represent veins. Results for TAWSS and OSI for the α and β branches of the small arteries and veins are shown in the bottom row

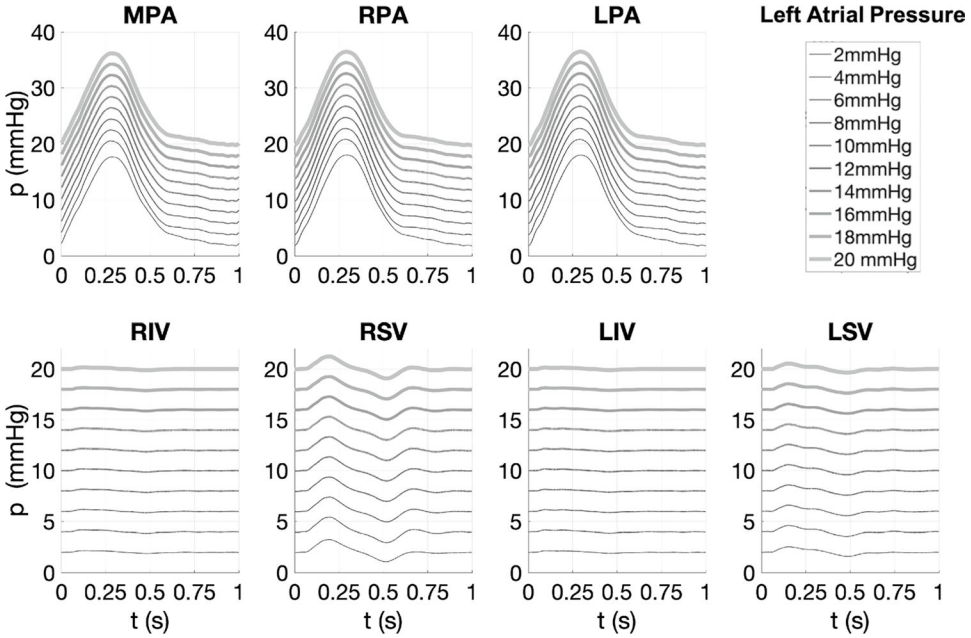

Fig. 6.

Predicted pressure at the midpoint of the large arteries (MPA, RPA, LPA) and large veins (RIV, RSV, LIV, LSV) with an elevated left atrial filling pressure that ranges between 2 mmHg and 20 mmHg

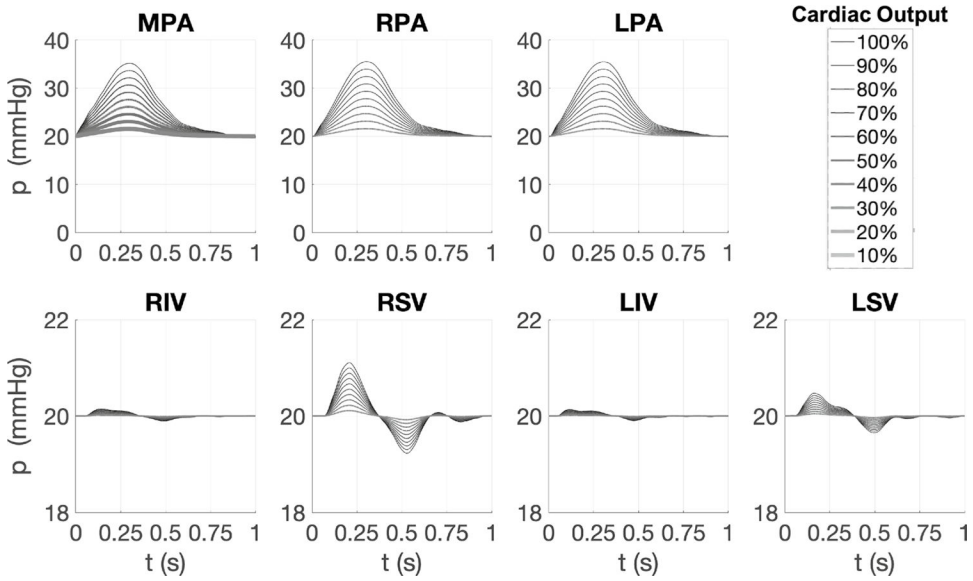

Fig. 7.

Predicted pressure at the midpoint of the large arteries (MPA, RPA, LPA) and large veins (RIV, RSV, LIV, LSV) with an elevated left atrial of 20 mmHg and a decreasing cardiac output that ranges from 100 to 10% of the normotensive inflow

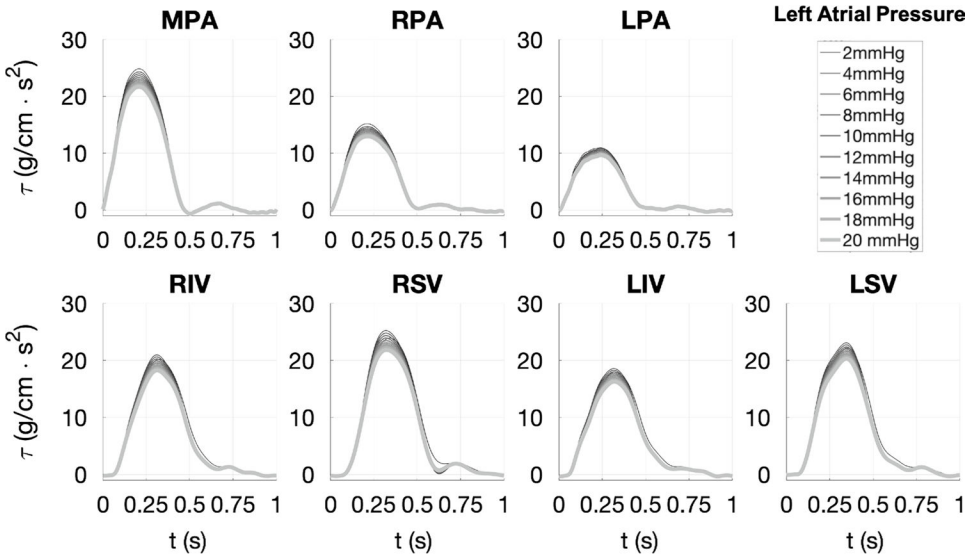

Fig. 8.

Shear stress using a boundary layer formation along three locations along the large arteries (MPA, RPA, LPA) and all four large veins for left atrial pressure ranging from 2 mmHg to 20 mmHg and normotensive cardiac output

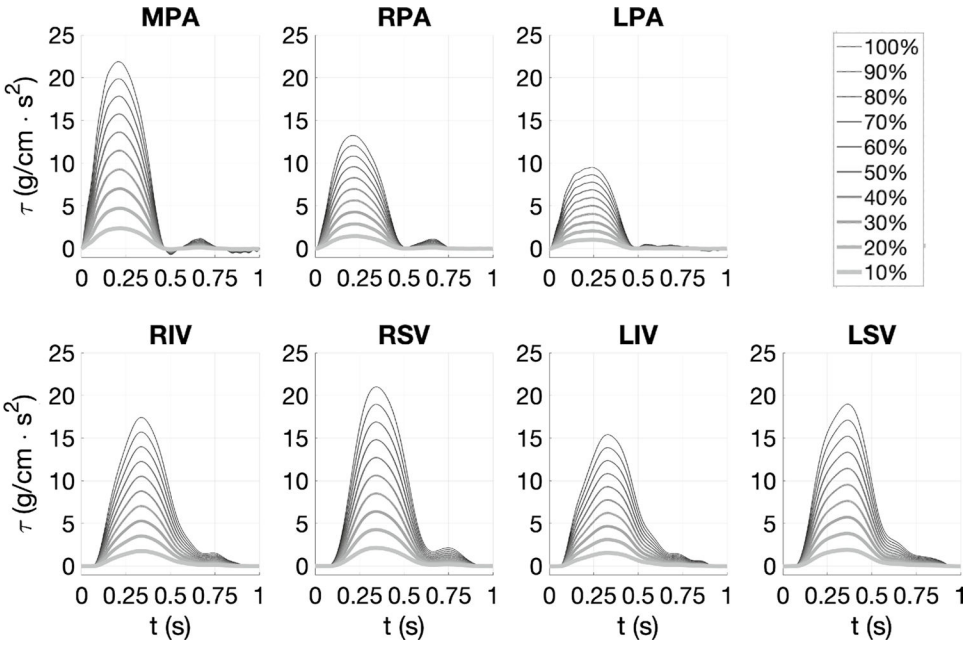

Fig. 9.

Shear stress using a boundary layer formation along three locations along the large arteries (MPA, RPA, LPA) and all four large veins for left atrial pressure of 20 mmHg and decreasing cardiac output

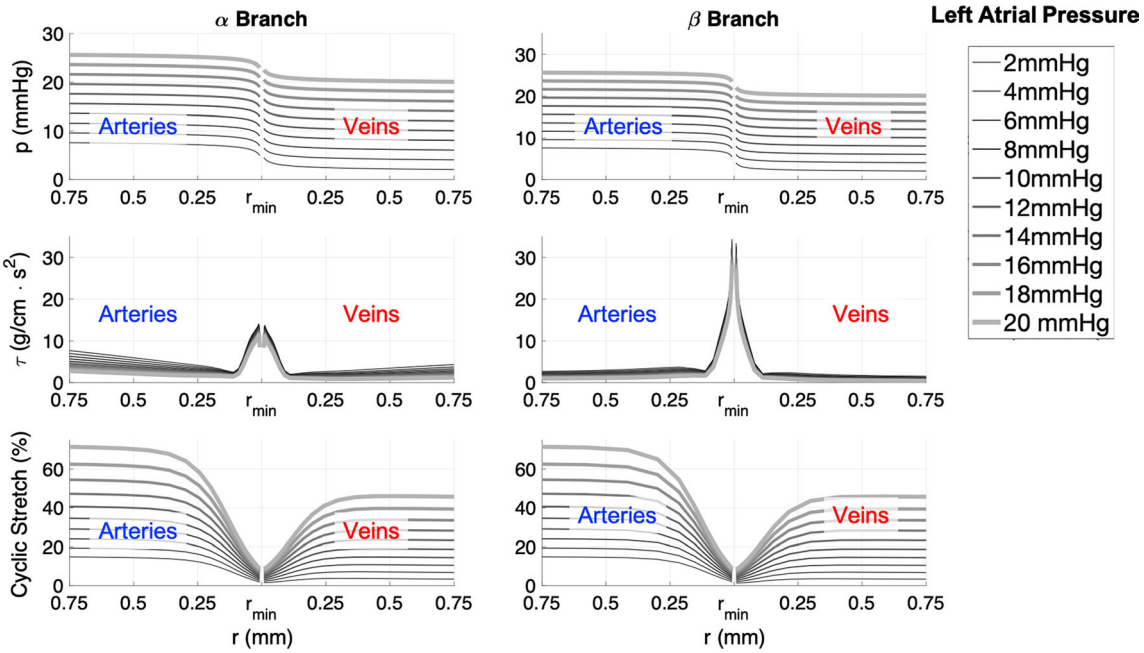

Fig. 10.

Mean flow, pressure, and cyclic stretch for the α branch (left) and β branch (right) for small arteries and veins of the structured tree. Here, the left atrial pressure ranges from 2 mmHg to 20 mmHg. The gaps in the pressure plots are due to the minimum radius, r_{min}, that is set in the model. There are fewer vessels in β branch, which leads to a larger gap being shown

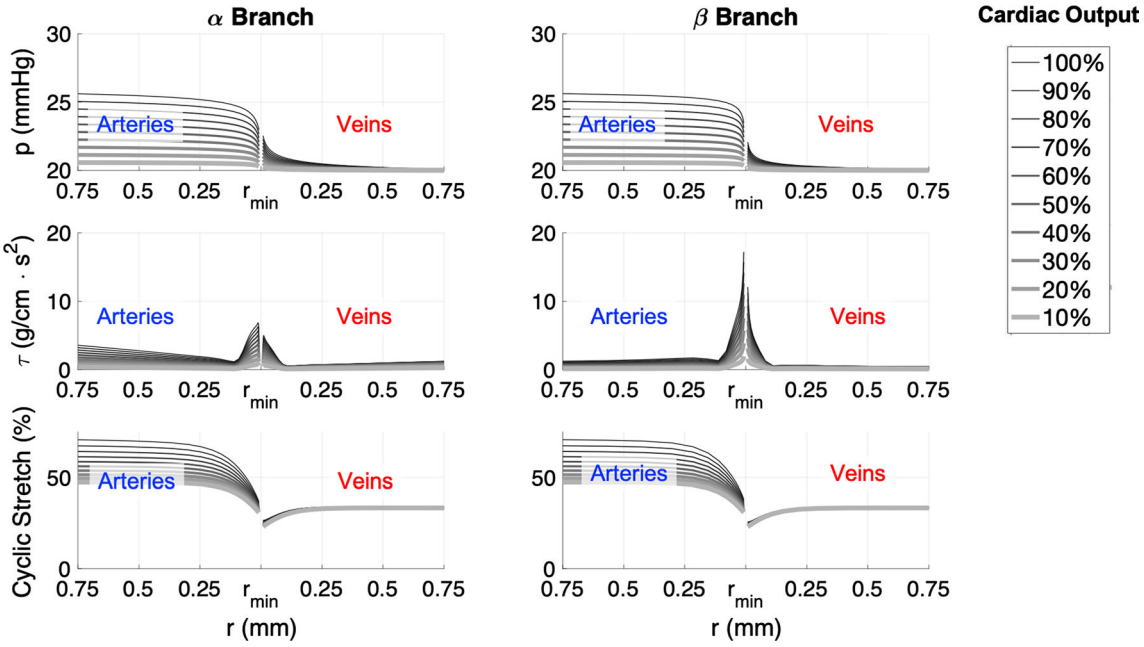

Fig. 11.

Mean flow, pressure, and cyclic stretch for the α branch (left) and β branch (right) for small arteries and veins of the structured tree. We impose a left atrial pressure of 20 mmHg and decrease the cardiac output by scaling the measured inflow waveforms between 10 and 100%. The gaps in the pressure plots are due to the minimum radius, r_{min}, that is set in the model. There are fewer vessels in β branch, which leads to a larger gap being shown

Table 1

List of parameters and variables

Quantity	Definition	Units	Value
Parameters			
T	Length of the cardiac cycle	s	1
ρ	Blood density	g/cm^3	1.057 Riches et al. (1973)
μ_L	Viscosity for large vessels	g/cm S	3.2 Pries et al. (1992)
$\mu_S(r_0)$	Viscosity for small vessels	g/cm S	see equation (2.11)
υ	Kinematic viscosity	cm^2/s	μ/ρ
δ	Boundary layer thickness	cm	$\sqrt{\upsilon T/2\pi}$ Lighthill (1975)
r_0	Given reference radius	cm	see Table 2
E	Young's modulus	mmHg	see equation (2.8)
h	Wall thickness	cm	see equation (2.8)
$r_{\min}$	Smallest vessel radius	mm	0.0075 Townsley (2012)
l_{rr}	Length to radius ratio	Dimensionless	15.75 (arteries); 14.54 (veins) Huang et al. (1996)
$(\alpha,\ \beta)$	Structured tree scaling factors	Dimensionless	(0.84,0.67) Chambers et al. (2020)
Variables			
$A(x,\ t)$	Instantaneous cross-sectional area	cm^2	computed
$q(x,\ t)$	Volumetric flow rate	cm^3/s	computed
$p(x,\ t)$	Blood pressure	mmHg	computed
$r(x,\ t)$	Instantaneous vessel radius	cm	computed
τ_w	Wall shear stress	g/(cm · s^2)	computed

Table 2

Dimensions of the large pulmonary vessels

Vessel name	Length (cm)	Radius (cm)
LSV	2.42	0.70
LIV	1.22	0.50
RSV	4.74	0.80
RIV	0.48	0.60
LTA	2.01	0.70
LIA	2.45	0.50
RTA	1.90	0.80
RIA	2.25	0.60
LPA	6.24	1.19
RPA	5.58	1.23
MPA	3.58	1.27

Main pulmonary artery (MPA), right (RPA) and left (LPA) pulmonary arteries, right (RIA) and left (LIA) interlobular arteries, right (RTA) and left (LTA) trunk arteries, right (RSV) and left (LSV) superior veins, and right (RIV) and left (LIV) inferior veins